JOURNAL OF GUIDANCE, CONTROL, AND DYNAMICS
Vol. 34, No. 3, May–June 2011

Longitudinal Flight Dynamics of Bioinspired Ornithopter Considering Fluid–Structure Interaction

Jun-Seong Lee* and Joong-Kwan Kim†
Korea Advanced Institute of Science and Technology, Daejeon 305-701, Republic of Korea
Dae-Kwan Kim‡
Korea Aerospace Research Institute, Daejeon 305-333, Republic of Korea
and
Jae-Hung Han§
Korea Advanced Institute of Science and Technology, Daejeon 305-701, Republic of Korea

DOI: 10.2514/1.53354

This paper addresses the flapping frequency-dependent trim flight characteristics of a bioinspired ornithopter. An integrative ornithopter flight simulator including a modal-based flexible multibody dynamics solver, a semiempirical reduced-order flapping-wing aerodynamic model, and their loosely coupled fluid–structure interaction are used to numerically simulate the ornithopter flight characteristics. The effect of the fluid–structure interaction of the main wing is quantitatively examined by comparing the wing deformations in both spanwise and chordwise directions, with and without aerodynamic loadings, and it shows that the fluid–structure interaction created a particular phase delay between the imposed wing motion and the aeroelastic response of the main wing and tail wing. The trimmed level flight conditions of the ornithopter model are found to satisfy the weak convergence criteria, which signifies that the longitudinal flight state variables of ornithopters need to be bounded and that the mean value of the variables are converged to the finite values. Unlike conventional fixed-wing aerial vehicles, the longitudinal flight state variables, such as forward flight speed, body pitch attitude, and tail-wing angle of attack in trimmed level flight, showed stable limit-cycle oscillatory behaviors with the flapping frequency as the dominant oscillating frequency. The mean body pitch attitude and tail-wing angle, and the root-mean-square value of the body pitch attitude, decreased as the flapping frequency increased. In addition, the mean forward flight speed is found to almost linearly increase with the flapping frequency.

Nomenclature

AST_k	=	aerodynamic strip, where k indicates the kth aerodynamic strip from wing root to wingtip
${}^{J_1}_{G}\mathbf{A}$	=	transformation matrix from local reference frame to global coordinate
b_{mw}	=	semispan of main wing
b_{tw}	=	tail-wing span
$c_{\mathrm{mw},k}$	=	main-wing chord length at kth aerodynamic strip
c_{tw}	=	tail-wing chord length
f	=	flapping frequency
$\dot{h}_{jk}$	=	local plunging motion velocity parallel to global z direction
M_{jk}	=	aerodynamic moment of kth aerodynamic strip
O_G	=	origin of global coordinate, where G indicates the global coordinate
$O_{\mathrm{mw},f}$	=	origin of local reference frame of main wing
${}^{J_1}_{G}\mathbf{r}_0$	=	position of local reference frame defined in global coordinate
${}^{P_k}_{J_1}\mathbf{r}_1$	=	position between J_1 and P_k (undeformed position) that is constant in local frame, where k indicates the index of point on the flexible body
${}^{P'_k}_{P_k}\mathbf{r}_2$	=	modal superposition vector in local reference frame
U	=	inflow speed or forward flight speed
w_B	=	vertical velocity of body center of gravity
Δt	=	numerical integration time step
θ	=	body pitch attitude
θ_{jk}	=	local pitch angle of kth aerodynamic strip; AST_k at jth time step
κ	=	main-wing motion or flapping-wing motion; upstroke is positive from midstroke plane to maximum flapping angle

Presented as Paper 2010-8237 at the AIAA Guidance, Navigation, and Control Conference, Toronto, 2–5 August 2010; received 8 December 2010; revision received 19 January 2011; accepted for publication 19 January 2011.

*Graduate Student, Department of Aerospace Engineering; jsl1009@kaist.ac.kr. Student Member AIAA.
†Graduate Student, Department of Aerospace Engineering; joongkwan.kim@kaist.ac.kr. Student Member AIAA.
‡Senior Researcher, Satellite Control System Department; dkk@kari.re.kr.
§Associate Professor, Department of Aerospace Engineering; jaehunghan@kaist.edu. Senior Member AIAA.

I. Introduction

AN ORNITHOPTER primarily consists of a pair of anisotropic flexible main wings attached to a flapping-wing motion mechanism and a tail. The role of the main wing in cruising flapping-wing flight is to produce enough lift and thrust for sustained flight, and the tail is used to balance the pitching moment with respect to the center of gravity [1]. To make the ornithopter a more useful flight platform for various practical tasks, its flight dynamics must be well understood. However, the complex couplings of unsteady low Reynolds number aerodynamics, wing kinematics, and the flexibility of the wings do not allow one to easily establish an accurate flight dynamics model of the ornithopter. Unlike insect-type flapping micro air vehicles (MAVs), the time scale of flapping frequency of larger bioinspired ornithopters is closer to the characteristic time scale of the vehicle's dynamic modes; therefore, the cycle-averaging method [2] for insect-type MAVs is no longer an effective tool for analysis of the flight dynamics of the ornithopter [3].

Assuming that the ornithopters have oscillatory behaviors in the longitudinal direction, instead of using a time-averaging sense, Dietl

and Garcia [3] studied the stability characteristics of limit-cycle oscillations (LCOs) of longitudinal flapping flight using a quasi-static aerodynamic model of a rigid flapping wing. Grauer and Hubbard [4] experimentally showed that the ornithopter has oscillatory flight dynamics with the flapping-wing frequency as the dominant oscillating frequency using state-of-the-art inertial measurement units mounted on a commercially available ornithopter. Later, they presented the simulation results showing similar oscillatory flight characteristics to the ornithopter by applying a simplified quasi-steady aerodynamic model and a nonlinear rigid multibody flight dynamic model [5]. Because the fluid–structure interaction (FSI) of ornithopter wings has not been taken into consideration, these previous studies have used further assumptions: the flapping- and twisting-wing motions were prescribed in [3], and the aerodynamic coefficients were tuned to keep trimmed flight in [5].

The main wing of ornithopters with large flapping motion undergoes elastic deformation incorporated with aerodynamics governed by an unsteady low Reynolds number flow. Such aeroelastic behaviors affect overall aerodynamic performance of the main wing as well as the flight dynamics of the ornithopter itself. Therefore, for the sound understanding of ornithopter flight dynamics (e.g., how an ornithopter can achieve stable flight without continuous control effort [4]), the FSI must inevitably be introduced in order to construct an integrative ornithopter flight simulation model.

Both modeling fidelity (accuracy) and computational cost (efficiency) should be considered together for a refined flight simulation of ornithopters that includes the effects of FSIs. Until now, the aerodynamic characteristics of flapping wings by themselves under predescribed wing kinematics have been actively studied to find the principles of unconventional aerodynamic mechanisms of nature's flyers under tethered conditions [6–8]. State-of-the-art high-fidelity modeling techniques, such as computational structural dynamics, computational fluid dynamics, and their coupling analysis, have aimed to investigate unique aerodynamic phenomena in flapping-wing flights; for example, the flexible wing has a higher thrust-to-power ratio than its rigid counterpart [6]. Reduced-order aerodynamic models, which can be effectively used for aeroelastic analyses of flapping wings, have been proposed [8–11]. However, simplified aerodynamics, such as quasi-steady aerodynamics, are still used, typically with a rigid-body dynamics model, to study flight dynamics characteristics of ornithopters [12–15]. Particularly, it is difficult to find literature about the flight dynamics of flapping-wing vehicles that consider wing flexibility and FSI.

This paper describes an integrative ornithopter flight simulator that includes a modal-based flexible multibody dynamics solver [16–18], a semiempirical reduced-order flapping-wing aerodynamic model [9–11], and their loosely coupled FSI to numerically simulate the ornithopter flight characteristics. The effect of FSI in ornithopter flight dynamics simulation is featured by comparing the spanwise and chordwise wing deformations, with and without aerodynamic loadings. Using the present flight simulator, Pfeiffer et al. [19] designed an ornithopter model and conducted flight dynamics simulations that considered FSI for a single flapping-wing frequency. This FSI analysis capability was also experimentally validated for a rectangular flapping-wing model in the literature [11].

The present study reports the stable LCO of flight states such as body pitch attitude, forward flight speed, and altitude of the ornithopter at the trimmed condition from the direct time integration of the ornithopter system model. Unlike previous works [3,5] where several simplifications were made to model system characteristics, wing flexibility and its aeroelastic interaction is considered in this study; wing deformations, such as passive, aeroelastic twisting motion, are not predefined but can be instantaneously calculated with respect to the change of flapping frequency, and the resultant transient effect on the vehicle motion can be evaluated. Similar to avian flight characteristics [20,21], the mutual relationships among the flapping frequency, the forward flight speed, and the behaviors of other flight states are explicitly presented in this paper.

The established ornithopter flight simulator can provide deeper insight into the flight dynamics of ornithopters by monitoring any flight state, which cannot be easily obtained in actual flight tests owing to the limited sensors, communications, and flight endurance times.

II. Ornithopter Modeling for Flight Dynamics Simulation

The primary task of the present paper is to simulate the flight dynamics of ornithopters considering FSI between anisotropic flexible-wing structures and a surrounding unsteady low Reynolds number flowfield. For those respective domains to be coupled and analyzed in an effective manner, a reduction approach in both structural and aerodynamic models is taken to realize an efficient FSI in a flight simulation environment. Figure 1 shows a simplified flowchart of the present integrative ornithopter flight simulator. The following sections provide a detailed modeling process and descriptions of the ornithopter flight simulator.

A. Structural Modeling of Main and Tail Wings

The ornithopter model used in this study has a natural quarter-ellipse wing shape with a wingspan of 540 mm and an aspect ratio of 5.58. The details of the material properties and dimensions of main-wing and tail-wing structures are summarized in Fig. 2 and Table 1 (in which LE denotes leading edge, CS denotes cross stiffener, STIF denotes stiffener, and EA denotes elastic axis). Also, the specifications of the ornithopter model drawn in Fig. 3 are listed in Table 2. This ornithopter model was virtually designed to be flyable in the presented flight simulator. An actual prototype was also manufactured based on this design, and it flew successfully afterward (Fig. 3a).

The structural design of a flexible flapping wing that has a particular patterned stiffener structure covered by thin skin was determined by iterative aeroelastic tailoring to obtain sufficient aerodynamic lift and thrust [19]. The finite element modeling of each

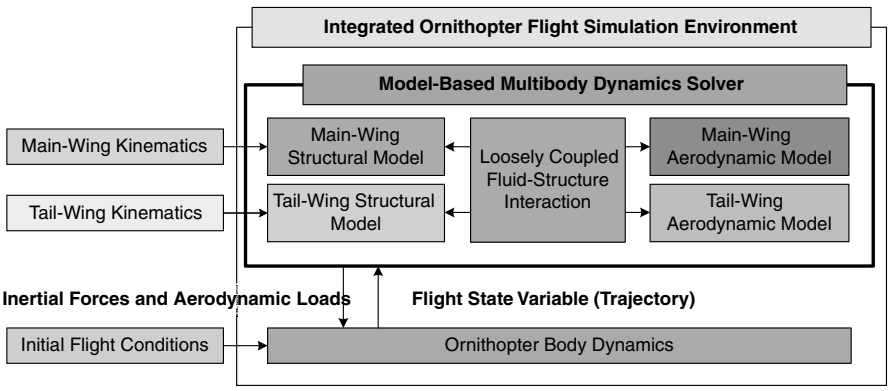

Fig. 1 Flowchart of integrative ornithopter flight simulator considering FSI of main wing and tail wing.

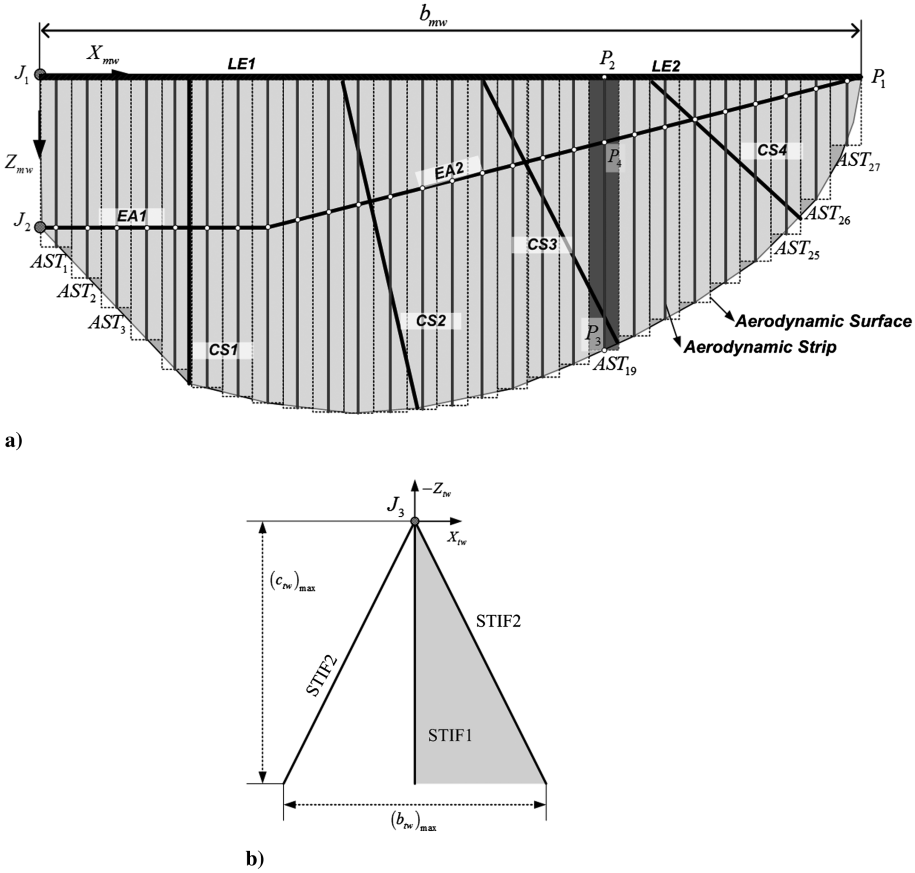

Fig. 2 Structural design of flexible ornithopter wings: a) main wing and b) tail wing.

wing structure was performed using ANSYS. The BEAM4 and SHELL63 elements in ANSYS were applied to the patterned stiffener structure made of carbon and the Ripstop nylon fabric skin of the wings, respectively. The BEAM4 is a three-dimensional elastic uniaxial element with tension, compression, torsion, and bending capabilities, and the SHELL63 is an elastic shell element that permits both in-plane and normal loads for membrane modeling. The elements have six degrees of freedom (DOFs) at each node. These elements were chosen to model all three-dimensional elastic behaviors of the carbon stiffener attached to nylon fabric skin, which underwent complex elastic deformation under root flapping motion (e.g., bending, twisting, and torsion modes). A total of 1857 finite elements were used to describe the structural dynamic response of the main wing. The structural model of a tail wing, shown in Fig. 2b, is relatively simple, and its finite element model was similarly constructed. The number of finite elements in the tail wing was 221, and the 196 nodal points were automatically seeded. The number of finite elements was chosen in a way that the modal solutions of interest could be converged; the number of elements was increased from a very coarse model to a dense one until modal solutions were converged.

Table 1 Material properties and dimensions of main and tail-wing structures

Part name	Elastic modulus, GPa	Poisson ratio	Density, kg/m^3	Thickness, mm
LE1	250	0.31	1800	2
LE2	100	0.31	1800	1
EA1 $\sim$ 2	175	0.31	500	0.4
CS1 $\sim$ 4	175	0.31	500	0.4
Main-wing skin	100	0.31	500	0.04
STIF1 $\sim$ 2	300	0.31	1495.42	0.5
Tail-wing skin	200	0.31	616.155	0.05

B. Flexible Multibody Dynamics and Coordinate Definitions

The elastic deformations of the main and tail wings are described in a local reference frame, which is attached to the undeformed wings, while the frame undergoes large, nonlinear global motion, i.e., flapping-wing motion and nonlinear oscillating body dynamics. The structural deformation of main and tail wings used in this study is represented by the linear combination of the mode shapes (fixed interface normal modes and component constraint modes for the Craig–Bampton method [17]). Figure 3b illustrates the definitions of the overall coordinate systems of the ornithopter used in this study. The point $O_{\mathrm{mw},f}$ is the origin of the local reference frame, and the point O_G is the origin of the global coordinate. The vector ${}^{J_1}_{G}\mathbf{r}_0$ indicates the position of the local reference frame defined in the global coordinate. The position vector ${}^{P_k}_{J_1}\mathbf{r}_1$ is constant and connects J_1 to P_k (undeformed position), expressed in the local frame. In this section, the subscript k specifies an index of a point on the flexible body. ${}^{J_1}_{G}\mathbf{A}$ is the transformation matrix from the local reference frame to the global coordinate. The translational deformation vector of P_k (P'_k is the deformed position of P_k) ${}^{P'_k}_{P_k}\mathbf{r}_2$ is a modal superposition vector. The deformed position or nodal point of the finite element model $\mathbf{r}_{P_k}$ is expressed in the global coordinate in Eq. (1):

$$\mathbf{r}_{P_k} = {}^{J_1}_{G}\mathbf{r}_0 + {}^{J_1}_{G}\mathbf{A}({}^{P_k}_{J_1}\mathbf{r}_1 + {}^{P'_k}_{P_k}\mathbf{r}_2) \tag{1}$$

Table 2 Specifications of the bioinspired ornithopter model

Parameter	Value	Parameter	Value
Total Mass	79.92 g	Tail-wing maximum span	0.12 m
Main-wing mass	7.68 g	Tail-wing maximum chord	0.12 m
Tail-wing mass	0.42 g	Main-wing span	0.54 m
Body mass	71.82 g	Main-wing mean chord	0.05 m
Main-wing area	0.044 m^2	Main-wing aspect	5.58
Tail-wing area	0.0072 m^2	Tail-wing aspect ratio	2

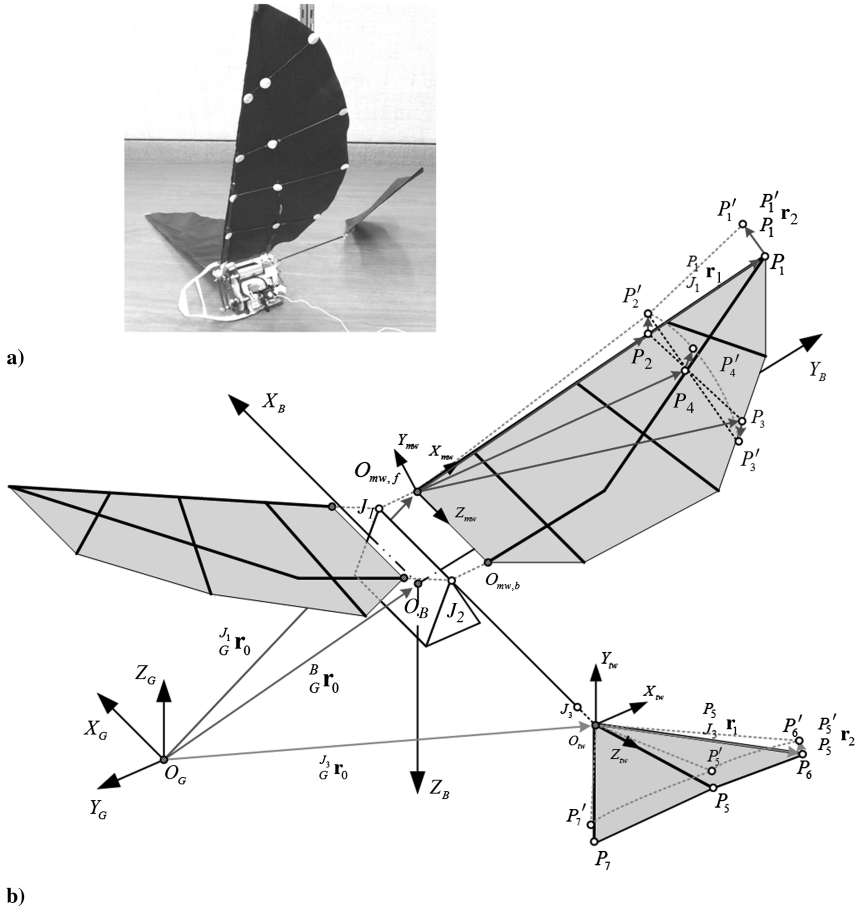

Fig. 3 Ornithopter model: a) prototype of designed model ornithopter and b) definition of ornithopter system coordinates.

Both J_1 and J_2 are coincident with the main-wing interface points, $O_{\mathrm{mw},f}$ and $O_{\mathrm{mw},b}$. The main-wing driving point J_1 has one-DOF motion, namely, the flapping-wing motion κ and the Z_{mw} are always parallel to X_B. Note that the flapping motion κ defined in Eq. (2) should be imposed gradually in both amplitude and frequency to prevent undesired, transient structural deformations at the initial stage of the flight simulation:

$$\kappa = \kappa_{\mathrm{MEAN}} + \kappa_1 \sin(2\pi\ \mathrm{ft}) \tag{2}$$

where the mean flapping angle κ_{MEAN} is set to 10 deg, the flapping-wing amplitude κ_1 is equal to 35 deg, and the flapping frequency f is varied from 6.5 to 16 Hz for this study.

The component mode synthesis and dynamic substructuring (particularly, the Craig–Bampton method [17]) with minor mathematical modification (mode shape orthonormalization) [18] is adopted in the flexible multibody dynamics solver (MSC.ADAMS) to calculate the elastic deformation of the flexible wings under a large flapping-wing motion. The fixed interface normal modes and the interface constraint modes with respect to the interface points (J_1 and J_2 in Fig. 2a) are extracted from the finite element models of main and tail wings for reduced-order structural modeling, and the finite element modeling software used in this study (ANSYS) generates this structural model in the form of a modal neutral file (MNF), which can be used directly in the flexible multibody dynamics solver as a flexible body. The MNF is a reduced-order structural model that is generated after the Craig–Bampton component mode synthesis method is applied to the model so that its DOFs are reduced based on the Craig–Bampton modal basis (fixed interface normal modes and component constraint modes). It contains information on reduced-order structural model, including 1) mass, 2) moment of inertia, 3) center of gravity, 4) reduced stiffness and mass matrix in terms of interface points, 5) fixed interface normal modes, and 6) interface constraint modes. The interface points are used to impose various boundary conditions, such as a flapping motion or constrained conditions. In this study, to represent the flexible multibody dynamics of flexible main-wing and tail-wing behavior, the first 25 and 3 normal modes were chosen for the main and tail wings, respectively. The number of modes for each wing was adjusted to accurately describe the dynamic behavior of the ornithopter and to reduce the total number of DOFs.

The governing equations for a flexible body can be derived from Lagrange's equations of the following form:

$$\frac{\mathrm{d}}{\mathrm{d}t}\left(\frac{\partial L}{\partial \dot{\xi}}\right) - \frac{\partial L}{\partial \xi} + \left[\frac{\partial \Psi}{\partial \xi}\right]^T \lambda - Q = 0, \qquad \Psi = 0 \tag{3}$$

where L is the Lagrangian (difference between kinetic energy and potential energy), Ψ is the constraint equations, λ is the Lagrange multipliers for the constraints, ξ is the generalized coordinates defined as $\xi = [\,{}^{J_1}_{G}\mathbf{r}_0 \quad \varphi \quad q\,]$ (φ denotes Euler angles and q denotes modal coordinates), and Q is the generalized applied force (projection to ξ space). Using Eq. (3), the governing differential equation of motion, in terms of the generalized coordinates, can be derived as follows:

$$\mathbf{M}\ddot{\xi} + \dot{\mathbf{M}}\dot{\xi} - \frac{1}{2}\left[\frac{\partial \mathbf{M}}{\partial \xi}\dot{\xi}\right]^T \dot{\xi} + \mathbf{K}\xi + \mathbf{f}_g + \left[\frac{\partial \Psi}{\partial \xi}\right]^T \lambda = \mathbf{Q} \tag{4}$$

where $\mathbf{M}$ is the time varying mass matrix, $\mathbf{K}$ is the generalized stiffness matrix, $\mathbf{f}_g$ is the generalized gravitational force, Ψ are the algebraic constraint equations, λ is the Lagrange multipliers for the constraints, and $\mathbf{Q}$ is the generalized applied forces. More detailed formulations on the modal-based flexible multibody dynamics can be found in [10,11].

C. Main-Wing and Tail-Wing Aerodynamic Models

1. Main-Wing Aerodynamic Model

The main-wing and flapping-wing aerodynamics are governed by an unsteady low Reynolds number (viscous) flow. In this paper, an improved version of the modified strip theory (MST) [10,11] that includes the dynamic stall model for large plunging wing motion is applied to the integrative ornithopter flight simulator. DeLaurier [9] proposed a design-oriented aerodynamic model for the unsteady aerodynamics of a flapping wing called the MST original, and its performance was examined by a manned ornithopter construction and flight tests. The core of the MST original is the modified Theodorsen function, or three-dimensional Theodorsen function, that takes into account a three-dimensional wake correction factor in terms of the wing aspect ratio and the reduced frequency. Also, the contributions of the section mean angle of attack, camber, partial leading edge suction, and friction drag were added, which allows MST original to be used for the calculation of the average lift, as well as the thrust, power required, and propulsive efficiency of a flapping wing in equilibrium flight. However, this model failed to predict the amplitude of the time-varying aerodynamic forces and moment according to the continuous flapping-wing motion that resulted from the application of the original MST that only classifies two types of flows: the attached flow range and the poststall flow range.

Kim et al. [10,11] improved the MST original (now denoted as MST Improved) for flapping-wing motion with larger amplitudes and a low Reynolds number flow consideration from the static wind-tunnel testing data. Moreover, the classification of flow in MST improved is more refined as follows: 1) attached flow range, 2) dynamic stall range, and 3) poststall flow range. In MST improved, the dynamic stall range was added, and the dynamic stall criterion was established using the ratio between the inflow resultant velocity and the sectional flapping-wing motion velocity. When the criterion is satisfied, the flapping wing maintains the aerodynamic characteristics of the attached flow range until the resultant angle of attack is bounded by the double static stall angle of attack. The details of the formulation and limitations of the MST original and MST improved aerodynamic models can be found in [9–11].

Aerodynamic strips (ASTs), highlighted by the solid bold line in Fig. 2a, are divided equally along the wing span. The aerodynamic surface is a two-dimensional surface that has the same aerodynamic properties as the corresponding AST. The motion parameters of the AST are obtained from the flexible structural dynamics of coincident structural nodal points. The definition of the motion parameters used in the main-wing aerodynamic model is expressed in Fig. 4a. For example, the local pitch angle θ_{jk} represents the rotational angle of the AST in the span direction and, measured from the position vectors $\mathbf{r}_{P_2,j}$ and $\mathbf{r}_{P_4,j}$, it is defined in the global coordinate. The subscript j indicates the index of the time step, and k implies the number of ASTs, starting from 1 and moving through to 27 (from wing root to wingtip). In the flexible multibody dynamics solver, the position vector of structural nodal points can be easily measured at each time index j, which contains the rigid-body motion of the ornithopter fuselage, the main-wing flapping motion, the local structural dynamic deformation, and the local deformation due to the fluid–structural coupling in the global coordinate.

To obtain the motion parameters of the AST virtually attached to the structural surface, three points, P_2, P_3, and P_4, were chosen, as shown in Fig. 4a. To obtain the local pitch angle θ_{jk} in the global coordinate, the directional cosine presented in Eq. (5) was used, where $\hat{e}_{X_G}$ is a unit vector of the X_G coordinate. The superscript c in Eq. (6) indicates the camber, which can be derived in the same manner as local pitch angle:

$$\theta_{jk} = \cos^{-1}\{(\mathbf{r}_{P_2,j} - \mathbf{r}_{P_3,j}) \cdot \hat{e}_{X_G} / |\mathbf{r}_{P_2,j} - \mathbf{r}_{P_3,j}|\} \tag{5}$$

$$\theta^c_{jk} = \cos^{-1}\{(\mathbf{r}_{P_4,j} - \mathbf{r}_{P_3,j}) \cdot \hat{e}_{X_G} / |\mathbf{r}_{P_4,j} - \mathbf{r}_{P_3,j}|\} \tag{6}$$

Each sectional strip has three DOFs of motion: plunging, translating, and pitching. The translational motion of point P_2 on the leading edge can be neglected due to the small amount of deformation in the

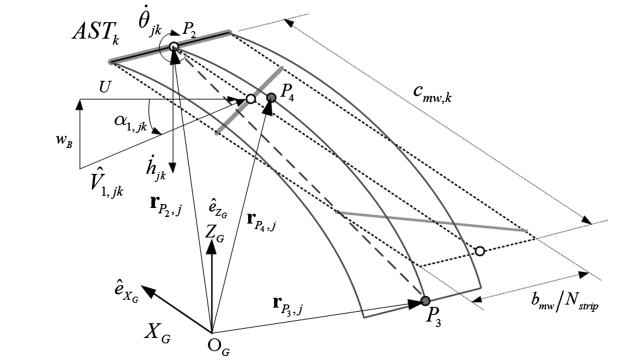

a)

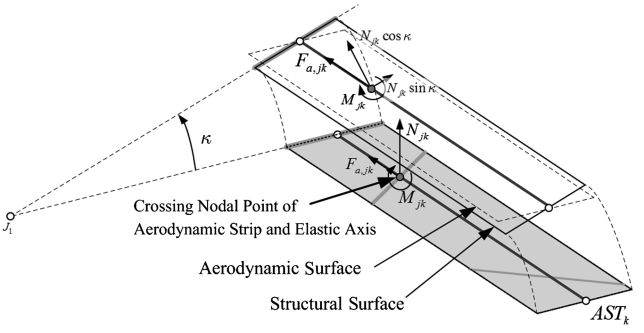

b)

Fig. 4 Aerodynamic forces and motion variables for main-wing aerodynamic model: a) definition of motion parameters for AST and b) definition of aerodynamic force and moment.

X_G direction. The plunging motion velocity $\dot{h}_{jk}$, calculated in Eq. (7), is parallel to the Z_G direction:

$$\dot{h}_{jk} = (\mathbf{r}_{P_2,j-1} - \mathbf{r}_{P_2,j}) \cdot \hat{e}_{Z_G} / \Delta t \tag{7}$$

The numerical integration time step Δt should be carefully determined based on the aeroelastic response of the flexible wings. In this study, the time step is set to 5 ms, which provides stable, converged solutions. Although the stability of the numerical differentiation is guaranteed by continuous wing structural motion, undesired motion might cause instability if sudden wing motions are applied during the initial simulation stage.

The definition of plunging motion $\dot{h}^*_{jk}$ in the aerodynamic model reveals motion perpendicular to the flapping axis or vehicle body attitude, not the motion perpendicular to the inflow velocity. Hence, the plunging velocity requires a coordinate transformation using the local pitch angle θ_{jk} and the body pitch attitude θ, as in Eq. (8):

$$\dot{h}^*_{jk} = \dot{h}_{jk} \cos(\theta_{jk} - \theta) \tag{8}$$

After the pitching and plunging motion parameters are determined using Eqs. (5) and (8), the sectional aerodynamics are able to be predicted. Moreover, the change of each aerodynamic surface area is small enough to neglect. The inflow speed or forward flight speed U and the vertical velocity of body w_B are parallel to the global coordinates X_G and Z_G, respectively (as shown in Fig. 4a).

The aerodynamic model computes the resultant force and moment vector at the intersecting point of the elastic axis and AST. In general, the elastic axis of an airplane wing is defined as the spanwise line along which the transverse load must be applied in order to allow only bending deformation, with negligible torsion of the wing at any section along the span. The elastic axis is sensitive to the boundary conditions of the structure and the applied loads. Thus, the process of determining the elastic axis, especially for ornithopter wings that have anisotropic flexibility with a thin skin and patterned structural stiffeners, is very complicated and requires much iteration. The stiffeners, EA1 and EA2 as shown in Fig. 2a, are the elastic axis of the

main-wing structural model, and they are iteratively determined through a finite element analysis (without a bending spanwise line under the application of wingtip torque).

For the FSI analysis, the sectional aerodynamic forces and moment are generally applied to the structural nodal point nearest to the elastic axis on the AST, as in Fig. 4b. The pitching moment was corrected to take into account the transformation of the moment reference point from the center of pressure to the elastic axis.

An important consideration in aerodynamic calculation is the aerodynamic surface transformation with respect to the flapping motion imposed at the joint J_1. When the undeformed structural surface is rotated with respect to the imposed flapping-wing motion, the aerodynamic surface is parallel to the global X_G-Y_G plane. The inclination angle between two undeformed surfaces is also called the flapping angle κ. The section normal force N_{jk} normal to the aerodynamic surface is transformed to the normal force on the structural surface $N_{jk}\cos\kappa$ and the spanwise tangential force $N_{jk}\sin\kappa$.

The section normal forces in Eq. (9) are composed of the circulatory force and noncirculatory force, such as the apparent mass effect. The sectional axial force F_a in Eq. (10) includes the leading-edge suction force of the oscillating wing, the frictional drag, and the camber-induced drag. The moment in Eq. (11) is also calculated similarly. These forces change with the flow criteria in MST improved [10,11]:

$$N_{jk} = N_{\text{circulatory},jk} + N_{\text{noncirculatory},jk} \tag{9}$$

$$F_{a,jk} = T_{S,jk} - D_{c,jk} - D_{f,jk} \tag{10}$$

$$M_{jk} = M_{ac,jk} + M_{\text{circulatory},jk} + M_{\text{noncirculatory},jk} \tag{11}$$

2. Tail-Wing Aerodynamic Model

Unlike the insect and bat, tailless ornithopters and birds are not common. The tail wing has an important role in the trimmed ornithopter flight in terms of balancing the instantaneous pitching moment with respect to the center of gravity. Because of the continuous flapping-wing motion, the pitching moment at the center of gravity has nonlinear, periodic, time-varying properties. Once the mean pitching moment has a nonzero value for each flapping period, the longitudinal dynamics will eventually diverge. However, the tail-wing aerodynamic modeling has not yet been investigated with regard to balancing the pitching moment. Previous research on tail-wing aerodynamics has been primarily focused on the tail-wing planform effects on the static aerodynamic characteristics [22].

In Pfeiffer et al.'s previous research on the longitudinal flight dynamics of the ornithopter [19], the tail-wing aerodynamic model was simplified to have a linear relationship between the aerodynamic lift and the tail-wing elevation angle. Thus, the tail-wing aerodynamic model passively affects the ornithopter system as a proportional linear feedback control. In this study, the tail-wing aerodynamic model was improved in a nonaffine form with respect to the tail-wing elevation angle, and the resultant velocity and new effective angle of attack are defined for the tail wing. The tail-wing aerodynamic model is acting as a feedback controller, albeit much more elaborate compared with the previous one, due to the inclusion of flight state variables, such as body pitch attitude, pitch rate, flight velocity vector, etc.

The detailed derivation of the tail-wing aerodynamic model for an bioinspired ornithopter is summarized in the Appendix. The resultant aerodynamic forces acting on the tail wing and the pitching moment with respect to the center of gravity are noted in Eqs. (12–14):

$$L_{\text{tw}} = \tfrac{1}{2}\rho U \hat{V}_{0.25\bar{c}_{\text{tw}}} \cdot S_{\text{tw}} \cdot C^*_{L,\text{tw}}(\alpha^*) \tag{12}$$

$$D_{\text{tw}} = D_{p,\text{tw}} + \frac{L_{\text{tw}}^2}{0.5\rho \hat{V}_{0.25\bar{c}_{\text{tw}}} S_{\text{tw}} \pi e \text{AR}} \tag{13}$$

$$\sum dM_{\text{CG,tw}} = dM_{\text{tw}} + (l_{\text{tw},z}dD_{\text{tw}} - l_{\text{tw},x}dL_{\text{tw}})\cos(\hat{\alpha}_{0.25\bar{c}_{\text{tw}}} + \theta) - (l_{\text{tw},x}dD_{\text{tw}} + l_{\text{tw},z}dL_{\text{tw}})\sin(\hat{\alpha}_{0.25\bar{c}_{\text{tw}}} + \theta) \tag{14}$$

Note that the only the control parameter for the tail wing is the tail-wing mean deflection angle δ_e, which is resolved inside the $M_{\text{CG,tw}}$ in a nonlinear form. Therefore, the tail-wing pitching moment with respect to the center of gravity is very difficult to express in affine form, and the nonlinear flight simulation by direct time integration shows the tail-wing effect on the trajectory of ornithopter flight dynamics.

D. Fluid–Structure Interaction of Flexible Wings

The spanwise and chordwise anisotropic wing flexibility allow a passive wing or an active wing to have proper wing bending and twisting interactions with the surrounding unsteady low Reynolds number fluid. In cooperation with the flexible multibody dynamics solver, the external aerodynamic forces and moment are automatically converted to the generalized coordinate of the governing differential equation of motion. In time step j, before proceeding to $j+1$, the number of iterations required to converge for the structural deformation to converge a certain range of error can be defined. Hence, the FSI procedure is loosely coupled, and the motion parameters and structural deformation obtained in time step j are used for $j+1$th aerodynamic calculations.

The flexible multibody dynamics solver was set to dynamics, and the gear stiff numerical integrator was chosen. The number of Newton–Raphson iterations for the convergence of the solution of Eq. (4) was fixed to a maximum of 10 for every time step, and the error bound was set to 1% during the iteration steps. The FSI framework used in this study has previously been experimentally validated for rectangular flapping-wing models [19].

To emphasize the FSI effect on the flapping wing, a center of gravity-constrained flight simulation was performed for two cases

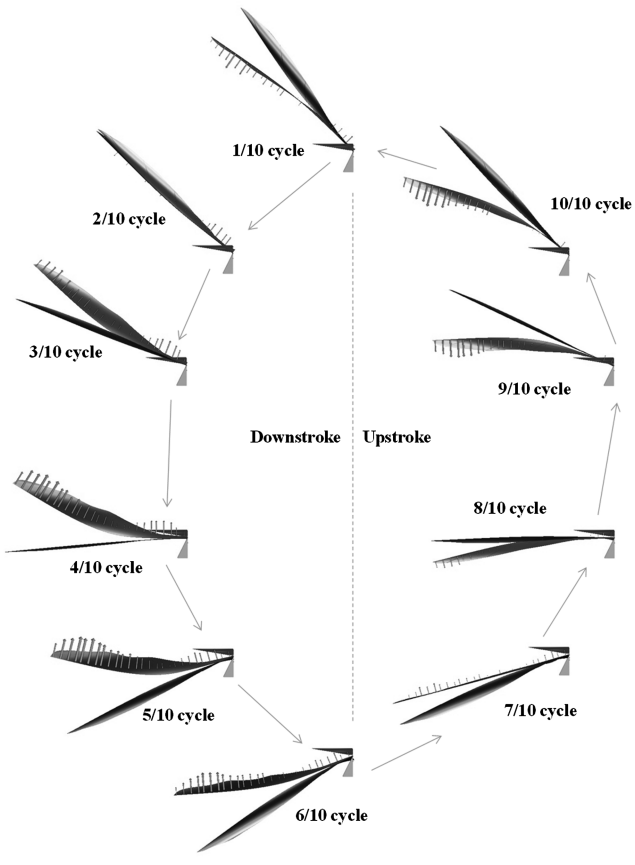

Fig. 5 Phase shift of structural deformation of flexible main wing due to FSI effect (flapping frequency: 12 Hz; vehicle attitude: 3.21 deg).

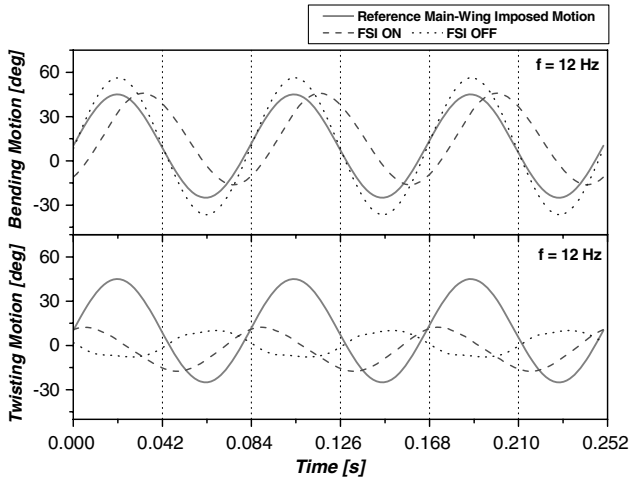

Fig. 6 Time history of wingtip bending motion and maximum twisting motion with and without FSI (reference signal: main-wing imposed motion; flapping frequency: 12 Hz; vehicle attitude: 3.21 deg).

analogous to wind-tunnel tests with/without ambient air: 1) FSI on (with aerodynamic loading) and 2) FSI off (without aerodynamic loading). The flapping frequency was set to 12 Hz, and the body pitch attitude was fixed to the mean trimmed flight condition at approximately 3.21 deg.

In Fig. 5, the shaded wing without the distribution of force vectors indicates the structural dynamic responses of the FSI-off wing. The two wings are synchronized to have identical flapping-wing motions. It clearly shows that the phase delay or advance effect is due to the applied aerodynamic loads. To compare the fluid structural response of the two wings more quantitatively, the wingtip point P_1 in Fig. 3b and the 19th AST, which has the maximum twisting deformation, were selected. The imposed flapping-wing motion, as a reference signal, was compared with the wing bending motion of P_1 and the twisting motion of AST_k, respectively (see Fig. 6). For point P_1, the FSI-on wing lags approximately 56 deg, and the FSI-off wing leads by approximately 4 deg. For the twisting motion at the 19th AST, the FSI-on wing leads by approximately 65 deg, and the FSI-off wing also leads by approximately 160 deg. If the reference signal is set as the FSI-off wing motion, then the FSI on each wing has approximately a 51.5 deg delay of wingtip bending motion and approximately a 91 deg delay of wing local twisting motion. The aerodynamic force is applied at the elastic axis, thus the magnitude of the twisting motion at the 19th strip has the same value of both the FSI-on and FSI-off wings. The phase angle of 91 deg has an important role in generating positive thrust between the 4/10 cycle and the 5/10 cycle, as shown in Fig. 5.

III. Longitudinal Trim Flight of Bioinspired Ornithopter

The integrative ornithopter flight simulator based on the loosely coupled FSI, explained in the previous section, is applied to tackle the trim flight dynamics of the ornithopter. The center of gravity is no longer constrained as in Sec. II.D in order to search for the trimmed free-flight conditions. In other words, the trim flight conditions for the ornithopter can be found using the same methods that are used for other types of aircraft. Finding the trim flight conditions for a wide range of flapping frequencies is beneficial in understanding the longitudinal flight dynamic characteristics of the ornithopter.

A. Trim Search Criteria for Longitudinal Level Flight

To simulate various hand-launching conditions (or initial flight conditions) of the ornithopter, a force vector with various magnitudes and directions is applied to the center of gravity for a certain period. Once the ornithopter is released with the initial flight conditions determined by an initial force vector, it automatically attempts to find a trimmed flight state using the harmony of its own aerodynamic lift, thrust, and moment. We found that the magnitude of the hand-launched force vector does not change the final trim flight speed and body pitch attitude, and the ornithopter shows only one trim flight condition for a specific flapping frequency. In other words, even though the ornithopter has different initial flight conditions, the trim flight condition is uniquely determined for a given flapping frequency. The initial conditions affect only the convergence time to the final trim condition. If the tail wing or another actuator of the

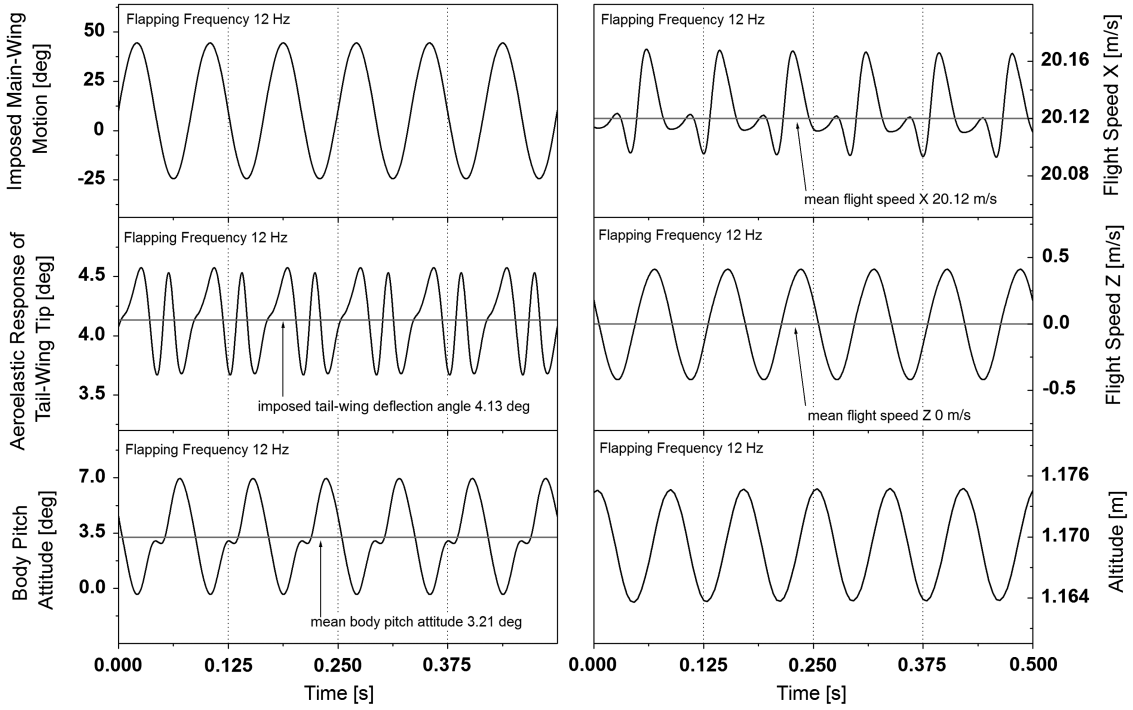

Fig. 7 Time history of longitudinal flight state variables: imposed main-wing motion, aeroelastic response of tail-wing tip, body pitch attitude, forward flight speed (flight speed *X*), vertical oscillating speed (flight speed *Z*), and altitude (flapping frequency: 12 Hz).

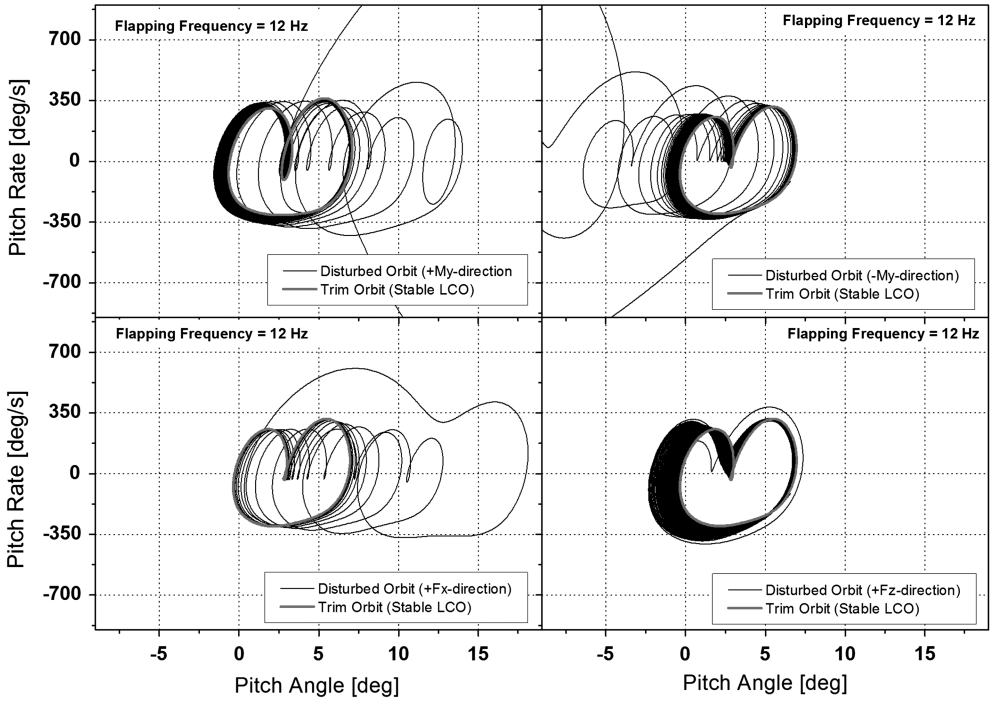

Fig. 8 Limit-cycle orbit recovery for pitching dynamics under external disturbances (flapping frequency: 12 Hz).

ornithopter are actively controlled, then there might be more than one trim condition. In this study, only the passive motion of a tail wing due to the flexibility is considered without any active tail-wing motions.

For a given flapping frequency, a trim mean tail-wing elevation angle δ_e must be found. Let x_i be any longitudinal flight dynamics state variable of the ornithopter, and the trimmed level flight condition can be expressed as Eqs. (15) and (16):

$$|\text{mean}[x_i(t)] - C_1| \to 0 \tag{15}$$

$$|x_i(t) - \text{mean}[x_i(t)]| \leq C_2 < \infty \tag{16}$$

where $t \in [nT, mT]$, $n < m$, $^{\forall}n$, $m \in \mathbb{Z}$, and for the arbitrarily real constant C_1 and C_2.

When the trim tail-wing elevation angle δ_e is to be found heuristically, flight states of the ornithopter are carefully monitored to see the criteria disclosed in Eqs. (15) and (16) are satisfied.

B. Trim Characteristics of Longitudinal Level Flight

1. Limit-Cycle Oscillation of Longitudinal Flight State Variables

It was observed from the flight simulation that the flight state variables of the ornithopter in trim show nonlinear dynamic behavior known as LCO; the LCO phenomena are not dependent on initial flight conditions within certain boundaries. In the case of flapping frequency of 12 Hz, Fig. 7 shows that the longitudinal flight state variables have the unique oscillatory behaviors satisfying Eqs. (15) and (16). The stability of the LCO is often studied by using the eigenvalues of the monodromy matrix in the Floquet theory [3]. In this study, however, the direct numerical simulation was performed to investigate the stability of LCO of the ornithopter. The aircraft stable trajectories were monitored in order to evaluate how the state trajectories converged to a LCO following the application of external force and moment disturbances. In the case of 12 Hz flapping-wing frequency, Fig. 8 shows that the pitching dynamics limit-cycle orbit in the phase plane returns to its original trim state, even after several kinds of disturbances are applied.

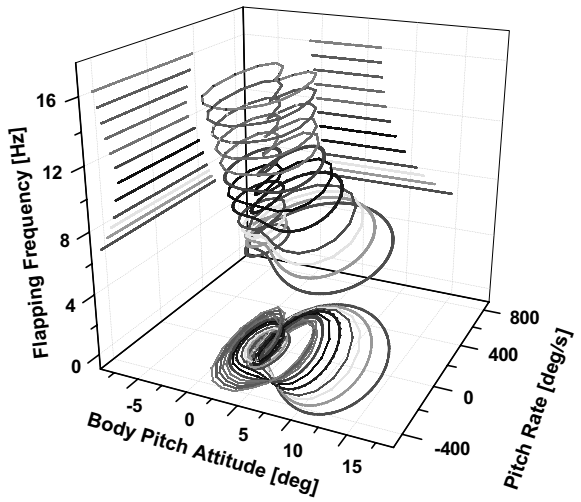

Fig. 9 Phase portraits of pitching dynamics of trimmed level flight ornithopter (flapping frequency: 6.5 ∼ 16 Hz).

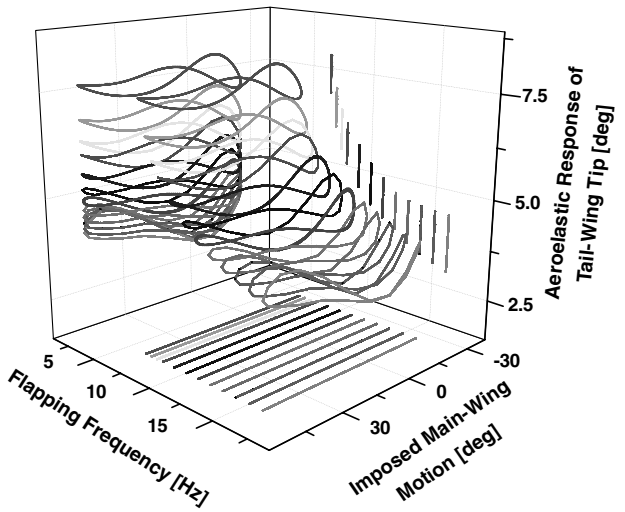

Fig. 10 Aeroelastic response of flexible tail-wing tip during trimmed level flight.

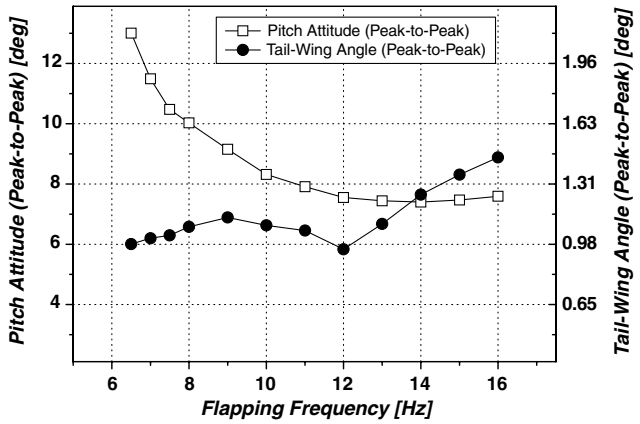

Fig. 11 Peak-to-peak values of pitch attitude and tail-wing angle vs flapping frequency.

The LCO is uniquely demonstrated for each trim condition in this study. The flapping frequency was adjusted from 6.5 to 16 Hz, and the corresponding trim flight state variables were found. In Fig. 9, the phase portraits for the pitching dynamics show the complex nonlinear dynamic behavior. As the flapping frequency increases (positive Z axis), the mean pitch angle is decreased and the inner closed loop in the phase portrait is dismissed as having a single closed loop for a higher flapping frequency. In other words, simplified pitching dynamics are obtained for higher flapping frequencies.

2. Tail-Wing Structural Vibration due to Main-Wing Motion

The structural response to the external forces is amplified when the natural frequency of the structure is tuned to the excitation frequency. The natural frequency of the first bending mode of the tail-wing structure is 31.75 Hz: sufficiently high compared with the ranges of the operational flapping frequencies. However, the pitch LCO contains higher harmonic forcing terms for the lower flapping frequency flight. There are flapping frequencies that are candidates to resonate the tail-wing structure, and the changes of phase portrait shapes shown in Fig. 10 are observed near the flapping frequencies of 9.0–10.0 and 14.0–15.0 Hz. As shown in Fig. 11, when the peak-to-peak values of the tail-wing aeroelastic response are increased according to the flapping frequency, the peak-to-peak values of the body pitch attitude are decreased; thus, the aeroelastic response of the tail wing might affect the passive flight stability of the ornithopter.

3. Mean Longitudinal Flight Dynamics of Trimmed Ornithopter

The trimmed level longitudinal flight of the ornithopter is summarized in Fig. 12, which shows the mean longitudinal flight state variables with respect to the flapping frequency. The mean values of the longitudinal flight state variables are calculated for the 10 cycles of flapping-wing motion. The observed state variables are the mean values of the tail-wing elevation angle, the forward flight speed, the body pitch attitude, and the peak-to-peak value of the body pitch oscillations. The mean tail-wing elevation angle is decreased as the flapping frequency increases. Hence, the mean flight speed is faster for the higher flapping frequency due to the reduced drag on the tail. The pitching dynamics associated with the flapping frequency can be solved from the data presented in Figs. 11 and 12. The mean body pitch attitude is almost inversely proportional to the flapping frequency. Interestingly, the peak-to-peak value of the pitch oscillation is also decreased with an increase of the flapping frequency up to 14 Hz. In the avian trim flight dynamics, the flapping frequency is adjusted to have the minimum power required for the actuation of wings with respect to the flight speed, and the wing beat amplitude and downstroke angular velocity are proportional to the airspeed or flight speed [20,21]. The ornithopter has symmetric upstroke and downstroke wing motion, unlike avian flight; however, ornithopters have similar mean flight dynamic characteristics to avian flight: the body pitch attitude and tail angle of attack are decreased as the air speed or flapping frequency increased.

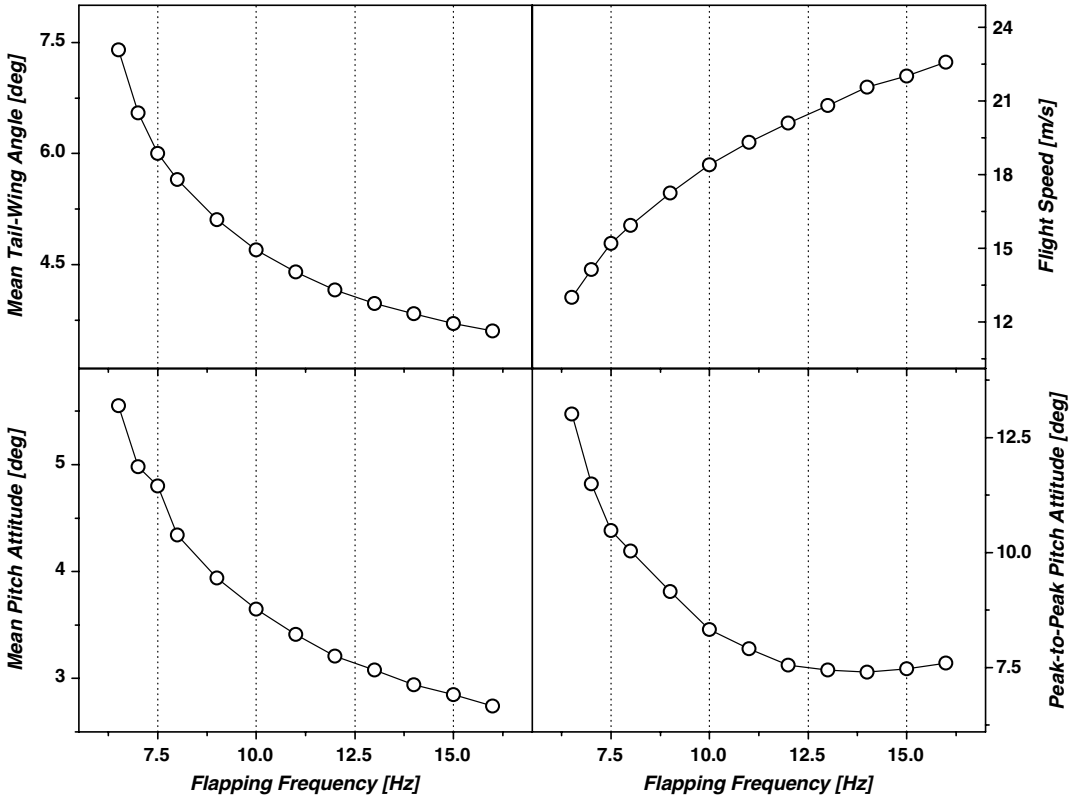

Fig. 12 Mean characteristics of trimmed flight state variables with respect to flapping-wing frequency.

IV. Conclusions

In this paper, an integrative ornithopter flight dynamics simulator including the modal-based flexible multibody dynamics solver has been introduced, and the refined flapping-wing aerodynamic model has been corrected for a low Reynolds number regime. The FSI effects were clearly demonstrated by comparing wing deformations with and without aerodynamic loadings. The trim condition for the stable longitudinal level flight was also investigated. From the simulation of an ornithopter model, the following was found. First, the trim flight conditions are uniquely determined once the flapping frequency is fixed (frequency-dependent trim flight characteristics). Second, the bioinspired ornithopter has unique trimmed flight dynamics characteristics LCO, and due to the LCO characteristics, the ornithopter shows robustness to external disturbances under continuous flapping. Finally, the mean flight dynamics of the trimmed ornithopter have functional relationships with respect to the flapping-wing frequency (e.g., mean pitch attitude is almost inversely proportional to the flapping frequency, and the peak-to-peak value of the pitch oscillation generally decreased with an increase of the flapping frequency).

The proposed integrative ornithopter flight simulator and trim search method will be helpful to systematically design ornithopters for unmanned air vehicle mission profiles and to study flight dynamics and control behaviors of the ornithopters.

Appendix: Tail–Wing Aerodynamic Model for Bioinspired Ornithopter

The detailed derivation of the tail-wing aerodynamic model for the bioinspired ornithopter in Sec. II.C.2 is given here. Figure A1 describes the definition of the tail-wing and vehicle body motion parameters used in the proposed refined tail-wing aerodynamic model. The resultant velocity $\hat{V}_{0.25\bar{c}_{\text{tw}}}$, shown in Fig. A1b and in Eq. (A1), is composed of ornithopter forward flight speed U, the vertical velocity w_B, the body pitch rate-induced velocity at the three-quarter chord point $w_{q,0.75\bar{c}_{\text{tw}}}$ on the tail-wing surface, and the rate of tail-wing motion $\dot{\delta}_e$:

$$\hat{V}_{0.25\bar{c}_{\text{tw}}} = \sqrt{(\hat{V}_{t,0.25\bar{c}_{\text{tw}}})^2 + (\hat{V}_{n,0.25\bar{c}_{\text{tw}}})^2}$$
$$\hat{\alpha}_{0.25\bar{c}_{\text{tw}}} = \tan^{-1}(\hat{V}_{n,0.25\bar{c}_{\text{tw}}}/\hat{V}_{t,0.25\bar{c}_{\text{tw}}}) \tag{A1}$$

where

$$\hat{V}_{t,0.25\bar{c}_{\text{tw}}} = U\cos(\theta-\delta_e) - w_B\sin(\theta-\delta_e)$$
$$\hat{V}_{n,0.25\bar{c}_{\text{tw}}} = U\sin(\theta-\delta_e) + w_B\cos(\theta-\delta_e) + w_{q,0.25\bar{c}_{\text{tw}}} - 0.25\bar{c}_{\text{tw}}\dot{\delta}_e$$
$$w_{q,0.75\bar{c}_{\text{tw}}} = q\{{}^{J_3}_{B}l_x + \bar{c}_{\text{tw}}\cos\delta_e\}\cos\delta_e$$
$$w_{q,0.25\bar{c}_{\text{tw}}} = q\{{}^{J_3}_{B}l_x + 0.5\bar{c}_{\text{tw}}\cos\delta_e\}\cos\delta_e$$

various velocity components are combined to represent the bound vortex $d\Gamma_{0.25\bar{c}_{\text{tw}}}$ of the tail-wing section at the chord length $\bar{c}_{\text{tw}}$. The bound vortex is located at the quarter-chord of the mean chord location, and a basic assumption is made for the flow around the tail wing to be attached for overall ranges of angles of attack. Once the zero normal flow boundary condition on solid surfaces is satisfied in Eq. (A2) at the control point of the three-quarter chord location from the joint, J_3 is reduced to the bound vortex $d\Gamma_{0.25\bar{c}_{\text{tw}}}$ in Eq. (A3). The normal velocity on the tail-wing surface $\hat{n}_{0.75\bar{c}_{\text{tw}}}$ is also defined in Fig. A1a:

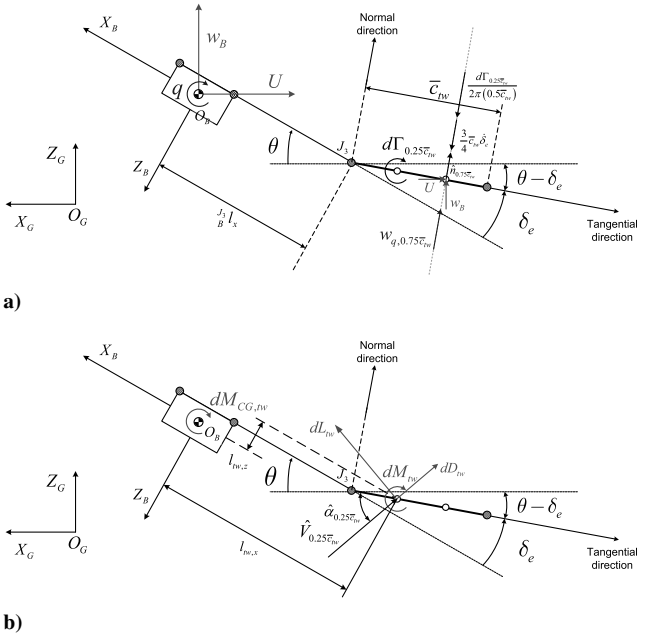

a)

b)

Fig. A1 Aerodynamic forces and motion variables for tail-wing aerodynamic model: a) definition of tail-wing and body motion parameters and lumped bound-vortex consideration of the tail wing for the tail-wing aerodynamic model; and b) directions and locations of aerodynamic forces and moment around tail wing and the pitching moment at the center of gravity due to tail-wing aerodynamic loads.

$$\hat{n}_{0.75\bar{c}_{\text{tw}}} = 0 = -\frac{d\Gamma_{0.25\bar{c}_{\text{tw}}}}{2\pi(0.5\bar{c}_{\text{tw}})} - \frac{3}{4}\bar{c}_{\text{tw}}\dot{\delta}_e + U\sin(\theta-\delta_e) + w_B\cos(\theta-\delta_e) + w_{q,0.75\bar{c}_{\text{tw}}} \tag{A2}$$

$$d\Gamma_{0.25\bar{c}_{\text{tw}}} = \pi\bar{c}_{\text{tw}}\left[U\sin(\theta-\delta_e) + w_B\cos(\theta-\delta_e) + w_{q,0.75\bar{c}_{\text{tw}}} - \frac{3}{4}\bar{c}_{\text{tw}}\dot{\delta}_e\right] \tag{A3}$$

The derivation of the bound vortex in Eq. (A3) and the resultant velocity in Eq. (A1) are assumed to be applied for a two-dimensional wing; then, the circulatory force on the tail wing can be obtained from the Kutta–Joukowski theorem. In Eq. (A4), it can be confirmed that the constitution of the two-dimensional lift of the tail wing is a multiplication of the dynamic pressure, lift slope, 2π derived in two-dimensional thin airfoil theory, and the new fictitious angles of attack α^*, shown inside the parentheses in Eq. (A4):

$$dL_{\text{tw}} = \rho\hat{V}_{0.25\bar{c}_{\text{tw}}}d\Gamma_{0.25\bar{c}_{\text{tw}}} = \frac{1}{2}\rho U\hat{V}_{0.25\bar{c}_{\text{tw}}}\cdot\bar{c}_{\text{tw}}\cdot\underbrace{2\pi\overbrace{\frac{[\sin(\theta-\delta_e) + (w_B/U)\cos(\theta-\delta_e) + (w_{q,0.75\bar{c}_{\text{tw}}}/U) - (3/4)(\bar{c}_{\text{tw}}\dot{\delta}_e/U)]}^{\alpha^*}}}_{c_{l,\text{tw}}} \tag{A4}$$

The extension of two-dimensional aerodynamic lift in Eq. (A4) to three-dimensional can simply be implemented by the modification of the lift slope 2π. Once the spanwise distribution of the circulation is assumed to be an elliptical distribution, then the lift acting on the tail wing L_{tw} is finally derived in Eq. (A5). The finite wing induces the downwash distribution along the tail-wing span, and the downwash generates drag called induced drag. The total drag of the tail wing D_{tw} consists of both the induced drag and the profile drag, or skin friction, in Eq. (A5). In a quasi-steady aerodynamic sense, once the aerodynamic coefficients $C^*_{L,\text{tw}}$ are known, then the instantaneous aerodynamic coefficients can be obtained according to the angle of attack α^*:

$$L_{\text{tw}} = \frac{e\text{AR}}{2+e\text{AR}} dL_{\text{tw}} b_{\text{tw}} = \frac{1}{2}\rho U \hat{V}_{0.25\bar{c}_{\text{tw}}} \cdot S_{\text{tw}} \cdot 2\pi \frac{e\text{AR}}{2+e\text{AR}} \alpha^*$$
$$= \frac{1}{2}\rho U \hat{V}_{0.25\bar{c}_{\text{tw}}} \cdot S_{\text{tw}} \cdot C^*_{L,\text{tw}}(\alpha^*)$$
$$D_{\text{tw}} = D_{p,\text{tw}} + \frac{L^2_{\text{tw}}}{0.5\rho \hat{V}_{0.25\bar{c}_{\text{tw}}} S_{\text{tw}} \pi e\text{AR}} \tag{A5}$$

The tail-wing moment M_{tw} in Eq. (A6) is negligible compared with the other components in relation to its contribution to the pitching moment at the center of gravity. Figure A1b illustrates the free-body diagram of the tail-wing forces and moment to estimate the pitching moment in Eq. (A6) with respect to the center of gravity:

$$\sum dM_{\text{CG,tw}} = dM_{\text{tw}} + (l_{\text{tw},z} dD_{\text{tw}} - l_{\text{tw},x} dL_{\text{tw}}) \cos(\hat{\alpha}_{0.25\bar{c}_{\text{tw}}} + \theta)$$
$$- (l_{\text{tw},x} dD_{\text{tw}} + l_{\text{tw},z} dL_{\text{tw}}) \sin(\hat{\alpha}_{0.25\bar{c}_{\text{tw}}} + \theta) \tag{A6}$$

where

$$l_{\text{tw},z} = {}^{J_3}_{B} l_z + 0.25\bar{c}_{\text{tw}} \sin\delta_e, \qquad l_{\text{tw},x} = {}^{J_3}_{B} l_x + 0.25\bar{c}_{\text{tw}} \cos\delta_e$$

Acknowledgments

The authors gratefully acknowledge the financial support provided by the Agency for Defense Development's Unmanned Technology Research Center. The first and second authors would like to thank the Brain Korea 21 Project of 2010. The authors also thank anonymous reviewers and the Editor for their valuable comments and suggestions.

References

[1] Han, J.-H., Lee, J.-S., and Kim, D.-K., "Bio-Inspired Flapping UAV Design: A University Perspective," *Proceedings of SPIE: The International Society for Optical Engineering*, Vol. 7295, 2009, pp. 7295I1–7295I12. doi:10.1117/12.815337

[2] Doman, D. B., Oppenheimer, M. W., and Sigthorsson, D. O., "Wingbeat Shape Modulation for Flapping-Wing Micro-Air-Vehicle Control During Hover," *Journal of Guidance, Control, and Dynamics*, Vol. 33, No. 3, 2010, pp. 724–739. doi:10.2514/1.47146

[3] Dietl, J. M., and Garcia, E., "Stability in Ornithopter Longitudinal Flight Dynamics," *Journal of Guidance, Control, and Dynamics*, Vol. 31, No. 4, 2008, pp. 1157–1162. doi:10.2514/1.33561

[4] Grauer, J. A., and Hubbard, J. E., Jr., "Inertial Measurements from Flight Data of a Flapping-Wing Ornithopter," *Journal of Guidance, Control, and Dynamics*, Vol. 32, No. 1, 2009, pp. 326–331. doi:10.2514/1.37495

[5] Grauer, J. A., and Hubbard, J. E., Jr., "Multibody Model of an Ornithopter," *Journal of Guidance, Control, and Dynamics*, Vol. 32, No. 5, 2009, pp. 1675–1679. doi:10.2514/1.43177

[6] Shyy, W., Aono, H., Chimakurthi, S. K., Trizila, P., Kang, C.-K., Cesnik, C. E. S., and Liu, H., "Recent Progress in Flapping Wing Aerodynamics and Aeroelasticity," *Progress in Aerospace Sciences*, Vol. 46, No. 7, 2010, pp. 284–327. doi:10.1016/j.paerosci.2010.01.001

[7] Liu, H., "Integrated Modeling of Insect Flight: From Morphology Kinematics to Aerodynamics," *Journal of Computational Physics*, Vol. 228, No. 2, 2009, pp. 439–459. doi:10.1016/j.jcp.2008.09.020

[8] Smith, M. J. C., "Simulating Moth Wing Aerodynamics: Towards the Development of Flapping-Wing Technology," *AIAA Journal*, Vol. 34, No. 7, 1996, pp. 1348–1355. doi:10.2514/3.13239

[9] DeLaurier, J. D., "An Aerodynamic Model for Flapping-Wing Flight," *The Aeronautical Journal*, Vol. 97, No. 964, 1993, pp. 125–130.

[10] Kim, D.-K., Lee, J.-S., and Han, J.-H., "Improved Aerodynamic Model for Efficient Analysis of Flapping-Wing Flight," *AIAA Journal*, Vol. 49, No. 4, 2011, pp. 868–872. doi:10.2514/1.J050556

[11] Kim, D.-K., Lee, J.-S., Lee, J.-Y., and Han, J.-H., "An Aeroelastic Analysis of a Flexible Flapping Wing Using Modified Strip Theory," *Proceedings of SPIE: The International Society for Optical Engineering*, Vol. 6928, 2008, Paper 69281O. doi:10.1117/12.776137

[12] Shim, Y.-S., and Kim, C.-H., "Evolving Physically Simulated Flying Creatures for Efficient Cruising," *Artificial Life*, Vol. 12, No. 4, 2006, pp. 561–591. doi:10.1162/artl.2006.12.4.561

[13] Mouret, J.-B., Doncieux, S., and Meyer, J.-A., "Incremental Evolution of Target-Following Neuro-Controller for Flapping-Wing Animals," *Lecture Notes in Computer Science*, Vol. 4095, 2006, pp. 606–618. doi:10.1007/11840541_50

[14] Hedrick, T. L., and Daniel, T. L., "Flight Control in the Hawkmoth *Manduca Sexta*: The Inverse Problem of Hovering," *Journal of Experimental Biology*, Vol. 209, No. 16, 2006, pp. 3114–3130. doi:10.1242/jeb.02363

[15] Dickson, W. B., Straw, A. D., and Dickinson, M. H., "Integrative Model of *Drosophila* Flight," *AIAA Journal*, Vol. 46, No. 9, 2008, pp. 2150–2163. doi:10.2514/1.29862

[16] Liu, A. Q., and Liew, K. M., "Non-Linear Substructure Approach for Dynamic Analysis of Rigid-Flexible Multibody Systems," *Computer Methods in Applied Mechanics and Engineering*, Vol. 114, Nos. 3–4, 1994, pp. 379–396. doi:10.1016/0045-7825(94)90178-3

[17] Craig, R. R., Jr., and Bampton, M. C. C., "Coupling of Substructures for Dynamic Analysis," *AIAA Journal*, Vol. 6, No. 7, 1968, pp. 1313–1319. doi:10.2514/3.4741

[18] "Theoretical Backgrounds," *MSC.ADAMS/Flex User's Manual*, MSC Software, Santa Ana, CA, 2003, pp. 10–30.

[19] Pfeiffer, A. T., Lee, J.-S., Han, J.-H., and Baier, H., "Ornithopter Flight Simulation Based on Flexible Multi-Body Dynamics," *Journal of Bionic Engineering*, Vol. 7, No. 1, 2010, pp. 102–111. doi:10.1016/S1672-6529(09)60189-X

[20] Tobalske, B. W., Hedrick, T. L., and Biewener, A. A., "Wing Kinematics of Avian Flight Across Speeds," *Journal of Avian Biology*, Vol. 34, No. 2, 2003, pp. 177–184. doi:10.1034/j.1600-048X.2003.03006.x

[21] Park, K. J., Rosén, M., and Hedenström, A., "Flight Kinematics of the Barn Swallow (*Hirundo Rustica*) over a Wide Range of Speeds in a Wind Tunnel," *Journal of Experimental Biology*, Vol. 204, 2001, pp. 2741–2750.

[22] Thomas, A. L. R., "The Flight of Birds that have Wings and a Tail: Variable Geometry Expands the Envelope of Flight Performance," *Journal of Theoretical Biology*, Vol. 183, No. 3, 1996, pp. 237–245. doi:10.1006/jtbi.1996.0217